Science Bulletin 69 (2024) 823–832

Contents lists available at ScienceDirect

Science Bulletin

journal homepage: www.elsevier.com/locate/scib

Article

Accelerated marine carbon cycling forced by tectonic degassing over the Miocene Climate Optimum

Fenghao Liu [a], Jinlong Du [a], Enqing Huang [a,*], Wentao Ma [b], Xiaolin Ma [c], Lucas J. Lourens [d], Jun Tian [a]

[a] State Key Laboratory of Marine Geology, Tongji University, Shanghai 200092, China
[b] State Key Laboratory of Satellite Ocean Environment Dynamics, Second Institute of Oceanography, Ministry of Natural Resources, Hangzhou 310012, China
[c] State Key Laboratory of Loess and Quaternary Geology, Institute of Earth Environment, Chinese Academy of Sciences, Xi'an 710061, China
[d] Department of Earth Sciences, Faculty of Geosciences, Utrecht University, Utrecht CB 3584, Netherlands

ARTICLE INFO

Article history:
Received 10 July 2023
Received in revised form 7 December 2023
Accepted 8 December 2023
Available online 2 January 2024

Keywords:
Global warming
Eccentricity cycle
Carbon cycle
Low-latitude hydrological cycle

ABSTRACT

Global warming during the Miocene Climate Optimum (MCO, ~17–14 million years ago) is associated with massive carbon emissions sourced from the flood basalt volcanism and ocean crustal production. However, the perturbation of tectonic carbon degassing on the interaction between climate change and carbon cycle remains unclear. Here, through time-evolutive phase analysis of new and published high-resolution benthic foraminiferal oxygen ($\delta^{18}O$) and carbon ($\delta^{13}C$) isotope records from the global ocean, we find that variations in the marine carbon cycle lead the climate-cryosphere system ($\delta^{13}C$-lead-$\delta^{18}O$) on 405,000-year eccentricity timescales during the MCO. This is in contrast to the previously reported climate-lead-carbon ($\delta^{18}O$-lead-$\delta^{13}C$) scenario during most of the Oligo-Miocene (~34–6 million years ago). Further sensitivity analysis and model simulations suggest that the elevated atmospheric CO_2 concentrations and the resulting greenhouse effect strengthened the low-latitude hydrological cycle during the MCO, accelerating the response of marine carbon cycle to eccentricity forcing. Tropical climate processes played a more important role in regulating carbon-cycle variations when Earth's climate was in a warm regime, as opposed to the dominant influence of polar ice-sheet dynamics during the Plio-Pleistocene (after ~6 million years ago).

1. Introduction

The Miocene Climate Optimum (MCO) between ~17 and 14 million years (Ma) ago represents a major reversal in the long-term cooling trend of the past ~34 Ma since continental-scale ice sheets formed on Antarctica, during which the global mean surface temperature was ~3–4 °C warmer than in the pre-industrial era and atmospheric CO_2 was maintained at relatively high levels of 470–630 ppm (1 ppm = 1 μL/L) [1–7]. This warming was probably caused by carbon injection from the emplacement of Columbia River Basalt Group (CRBG), which was estimated to emit about 4090–5602 Pg (10^{15} g) carbon (equivalent to ~9–12 times fossil CO_2 emissions for 1850–2021) during the MCO [1,4,8–13]. Although high-precision geochronology shows that major phases of the CRBG were emplaced ~300 thousand years (ka) after the onset of the MCO [11], recent modelling result suggests that the crystallization of pre-eruption intrusions could release enough carbon to drive significant global warming [14]. However, the short-lived (more than 95% erupted between 16.7 and 15.9 Ma) and relatively small input of CO_2 from CRBG appear insufficient to explain the long-duration of the MCO [11,15]. The ~35% higher crustal production rates between ~18 and 14 Ma than modern could be another persistent driver of the strikingly warm climate [15]. As these temperature and CO_2 estimates are within the IPCC (The Intergovernmental Panel on Climate Change) projected pathways for 2100, the MCO is considered as a geological analogue for future warming scenarios [4,5] and serves as a valuable time window to investigate the interaction between carbon input and climate change.

Past changes in climate and carbon cycle on different time scales have been documented by the stable isotope composition of benthic foraminiferal oxygen ($\delta^{18}O$) and carbon ($\delta^{13}C$), as they are proxies for ice volume/deep-sea temperatures and carbon transfers between the ocean and other reservoirs, respectively [6,16,17]. On >10^5-year timescales, the 3-million-year MCO was characterized by a global benthic $\delta^{18}O$ minimum, reflecting the increase in deep-sea temperatures and the decrease in continental cryosphere [6,16,18]. Contemporaneous with the MCO, a long-lasting benthic $\delta^{13}C$ maximum, termed the Monterey Carbon

* Corresponding author.
E-mail address: ehuang@tongji.edu.cn (E. Huang).

https://doi.org/10.1016/j.scib.2023.12.052

Isotope Excursion (MCIE, ~16.7–13.6 Ma), has been recognized in the global ocean [19–21]. This ~1.0‰ positive $\delta^{13}C$ excursion has been attributed to increased burial of organic carbon on continental shelves due to global sea-level rise [4,21–23]. On 10^4–10^5-year timescales, Earth's orbital eccentricity is strongly imprinted in Cenozoic stable isotope, especially the most prominent 405-ka cycle in benthic $\delta^{13}C$ [6], which is likened to the "heart-beat" of Earth's climate system [24]. The MCIE consisted of eight carbon isotope maxima events paced by the 405-ka periodicity [19,21]. After the MCO, the 100 and 405 ka cycles almost faded away in benthic $\delta^{18}O$ [6,16], probably because the Antarctic ice sheets expanded, and the cryosphere became sensitive to obliquity forcing [6,25]. Until the last ~1 Ma, the 100-ka cycle again dominated the benthic $\delta^{18}O$ variability [6,16,26].

Previous studies have also shown that benthic $\delta^{18}O$ and $\delta^{13}C$ variations at the 100-ka eccentricity cycle were in phase throughout the Oligo-Miocene (~34–6 Ma), but antiphase during the Plio-Pleistocene (after ~6 Ma) [17,27]. This phase reversal corresponds to different Earth's climate regimes. When Earth was glaciated by unipolar ice sheets at Antarctica between ~34–6 Ma, eccentricity maxima tended to reduce the ice volume, leading to higher sea level and depletion of seawater $\delta^{18}O$ [17]. At the same time, eccentricity maxima could enhance monsoons and chemical weathering at low latitudes, resulting in land-to-ocean transfer of organic matter and depletion of deep-sea $\delta^{13}C$ [17]. However, when Earth entered into the bipolar ice sheets state after ~6 Ma [28], the shrinkage of Northern Hemisphere ice caps during eccentricity maxima could lead to reforestation of large continental areas [17], less dust transport from the Saharan/Asian interior to the ocean and thus decrease in marine biological pumping efficiency [29]. Together, these have resulted in an ocean-to-land transfer of isotopically light carbon (^{12}C) and further caused an antiphase relationship between benthic $\delta^{18}O$ and $\delta^{13}C$.

Although benthic $\delta^{18}O$ and $\delta^{13}C$ variations were basically in phase at the 100-ka cycle within the Oligo-Miocene, their leading and lagging relationship changed along with time and appeared to be modulated by the extremely long 2.4-Ma eccentricity cycle [17]. In general, due to the relatively long carbon residence time of ~65 ka in the ocean, benthic $\delta^{18}O$ variations precede those of $\delta^{13}C$ by ~1.9–2.5 ka at the 100-ka cycle [17,24,30,31]. However, over the maxima of 2.4-Ma cycle, changes in the Miocene benthic $\delta^{13}C$ were found to lead those of $\delta^{18}O$ at the 100-ka cycle [17]. It is concluded that a substantial enhancement of chemical weathering at low latitudes during extreme eccentricity maxima may accelerate the response of marine carbon cycle to orbital forcing, ultimately leading to the $\delta^{13}C$-lead-$\delta^{18}O$ scenario [17].

Characteristics of the 100-ka cycle in benthic $\delta^{18}O$ and $\delta^{13}C$ have been extensively discussed. Those of the 405-ka cycle, however, are largely unexplored. Similar to those occurred at the 100-ka cycle, benthic $\delta^{18}O$ and $\delta^{13}C$ varied nearly in phase at the 405-ka cycle during the Oligo-Miocene [17]. But it remains unknown whether there are shifts in their phase relationship at this eccentricity periodicity. The deep-sourced carbon emissions had caused significantly warm climatic conditions during the MCO, and the concurrent low-latitude monsoon precipitation and chemical weathering had also reached a peak [18,32–36]. Accordingly, the MCO greenhouse effect may have played a role similar to the extreme eccentricity maxima modulated by the 2.4-Ma cycle, which likely had caused a shift in the phase relationship between benthic $\delta^{18}O$ and $\delta^{13}C$ at the 405-ka cycle. This possibility has not yet been evaluated.

To address this issue, we analyze the time-evolutive phase relationship between benthic $\delta^{18}O$ and $\delta^{13}C$ throughout the Oligo-Miocene, based on eight published records from the International Ocean Discovery Program and its predecessor programs (IODP/ODP) and a new time-series from IODP U1505C. We then calculate the sensitivity of benthic $\delta^{18}O$ and $\delta^{13}C$ to orbital forcing to assess the sensitivity of cryosphere and marine carbon cycle to the 405-ka cycle. In addition, we use a 7-box biogeochemical model to investigate the response of marine carbon cycle to eccentricity forcing under a high CO_2 emissions background.

2. Materials and methods

2.1. IODP Site U1505

Four holes were cored at IODP Site U1505 (18°55.0570′N, 115°51.5370′E; water depth 2916.6 m) during the Expedition 368, located in the northern South China Sea [37] (Table S1 online). Holes A, B, and D penetrated only 184.5 m below the seafloor (depth referred to as the IODP CSF-B scale throughout the manuscript) and covered the Plio-Pleistocene, while Hole C was drilled to 480.2 m and extended to the early Oligocene. As a result, no parallel holes have been obtained to generate a spliced complete stratigraphic section for the Oligo-Miocene. A total of 45 biostratigraphic datums have been identified in Hole C, suggesting a succession from the early Oligocene to the Pleistocene without any apparent sedimentary hiatus. In this study, we analyzed samples from the interval between 345.5 and 122.2 m of Hole C.

2.2. Stable isotope analysis

All samples were collected at a depth resolution of 20 cm. Samples were oven-dried at 60 °C, weighed and soaked in water for 48 h, and washed through a 63 μm sieve. Residues were further dried at 60 °C, then weighed and sieved through a 150 μm sieve. Well-preserved specimens of epibenthic *Cibicidoides wuellerstorfi* and/or *Cibicidoides mundulus* with a shell size >400 μm were picked for the isotopic analysis.

After being crushed, fine-grained particles were removed from foraminiferal tests in alcohol in an ultrasonic bath. Isotope measurements were performed using a Thermo-Finnigan MAT 252/253 mass spectrometer at the State Key Laboratory of Marine Geology, Tongji University. The instrument is coupled to a Carbo-Kiel Device (Type IV) for automated CO_2 preparation. Samples were reacted with 99% H_3PO_4 at 70 °C. Results were calibrated against the National Bureau of Standard 19 and reported in per mil (‰) relative to Vienna Pee Dee Belemnite (VPDB). The long-term standard error is better than ±0.07‰ and ±0.04‰ for $\delta^{18}O$ and $\delta^{13}C$ analyses, respectively.

2.3. Chronology of Hole U1505C

(i) Biostratigraphy. A total of eight planktonic foraminiferal and thirteen calcareous nannofossil datums were identified in the 345.5–122.2 m depth interval during the shipboard analysis [37] (Tables S2 and S3 online). We performed a fourth-order polynomial fit to the depth-age tie points of planktonic foraminiferal and nannofossil datums, respectively (Fig. S1 online). These two polynomial relationships show a relatively large offset of ~0.2–3 Ma, with nannofossil datums always suggesting an older age model than foraminiferal datums. The nannofossil stratigraphy indicates a relatively stable sedimentation rate, while the foraminiferal stratigraphy implies more variable sedimentation rates.

(ii) Stable isotope stratigraphy. Pronounced and rapid changes in benthic foraminiferal $\delta^{18}O$ and $\delta^{13}C$ can serve as stratigraphic markers on a global extent [38–40]. We identified five $\delta^{18}O$ and six $\delta^{13}C$ stratigraphic markers by comparison with benthic $\delta^{18}O$ and $\delta^{13}C$ records from IODP/ODP Sites 1146, U1337 and 1264–1265 [6,17,19,30,34,41–46] (Fig. S2 and Table S4 online). The onset of the MCO was found at 298.77 m (~16.95 Ma) and marked by an

abrupt decrease in $\delta^{18}O$ by ~1‰ [18]. Within the MCO, the most pronounced $\delta^{18}O$ variation was marked by a rapid decrease of ~0.7‰ at 270.36 m (~15.58 Ma) and related to the Miocene Thermal Maximum [18,44,47]. The Middle Miocene Climate Transition was recognized at 236.79 m (~13.83 Ma), characterized by a ~1‰ positive excursion in $\delta^{18}O$ [42,44]. The Tortonian Thermal Maximum with a ~0.8‰ increase in $\delta^{18}O$ was discovered at 194.72 m (~10.78 Ma) [43,44]. An additional positive $\delta^{18}O$ shift (328.55 m, ~19.84 Ma) was identified after the MCO.

For the $\delta^{13}C$ stratigraphy (Fig. S2 and Table S4 online), the Late Miocene Carbon Shift starts at ~7.48 Ma (145.34 m) and ends at ~6.68 Ma (132.11 m) [48–50], while the Middle Miocene Carbon Shift lasts from ~13.65 Ma (232.28 m) to ~12.09 Ma (209.33 m) [20,44]. The onset of the first carbon isotope maxima event (292.01 m, ~16.68 Ma) and the end of the sixth carbon isotope maxima event (232.28 m, ~13.65 Ma) are well documented in our record [18,44,47]. An additional $\delta^{13}C$ minimum event was identified at 317.69 m (~18.78 Ma).

When plotted together, we find that the $\delta^{18}O$ and $\delta^{13}C$ stratigraphy is more consistent with the calcareous nannofossils datums rather than with planktonic foraminifera (Fig. S1 online). The reasons for the inconsistency between foraminiferal datums and other stratigraphic markers are unknown, but it may prompt a reconsideration of the foraminiferal stratigraphy at this site. Two calcareous nannofossil events (B *Reticulofenestra pseudoumbilicus*, 12.83 Ma; T *Sphenolithus heteromorphus*; 13.53 Ma) have been recognized at the same depth of 233.04 m [37]. The latter event appears to be more consistent with the stable isotope stratigraphy and is therefore adopted (Table S2 gray shadow online). Finally, we constructed an initial age model using a fourth-order polynomial applied to twelve calcareous nannofossil datums and eleven isotope age control points (Fig. S1 online).

(iii) Astronomical tuning. To provide a more refined chronology, we correlated the U1505C benthic $\delta^{18}O$ to other published high-resolution benthic $\delta^{18}O$ records (Fig. S3 online). These published results are from IODP/ODP Sites 1146 (~17.4–6 Ma), U1337 (~20–17 Ma) and 1264–1265 (~21–17 Ma) [6,17,19,30,34,41–46], whose age models were established using the astronomical tuning method based on biostratigraphy and magnetostratigraphy. Our $\delta^{18}O$ series was then manually aligned to the target datasets using the program of "QAnalyseries2.0.8" (Fig. S3 online) [51,52].

2.4. Time evolutive phase

The evolutive phase relationship was calculated using the cross-spectral fast Fourier transform analysis. This was implemented using the crossSpectrum function included in the IRISSeismic R package [53,54]. This method has been described in detail in Ref. [17]. We computed the cross spectra using a 1.2-Ma-wide window with a 0.2-Ma step and extracted the evolutive phase relationship in the 405-ka bands using a frequency range between 360 and 450 ka. In this study, we adopted the evolution phase results with a coherence of >0.6 (corresponding to a confidence level of ~97.5% of no-zero coherence).

2.5. Eccentricity sensitivity

We define the 405-ka eccentricity sensitivity (S_{ecc}) of a proxy as

$$S_{ecc} = \sigma^2_{proxy}/\sigma^2_{eccentricity}, \quad (1)$$

where σ^2_{proxy} is the eccentricity variance in the proxy records, in units of 10^{-6}, and $\sigma^2_{eccentricity}$ is the variance of the theoretical eccentricity solution. We quantified S_{ecc} using the multi-taper method of time–frequency power spectrum integration via the astrochron R package. Prior to analysis, proxy records were interpolated to evenly spaced sequences with a step equal to their original resolution. The eccentricity series was also resampled with a resolution equivalent to the proxy records. Long-term trends of the proxy records were removed from their respective 1 Ma window. We used 2π prolate data tapers for time–frequency analyses with a 1 Ma window and a 0.1 Ma step, and extracted the prominent 405-ka eccentricity signal from the frequency range between 360 and 450 ka. Details of the method and code can be found in Ref. [55].

2.6. Model description

(i) Physical scheme. Our biogeochemical box model consists of an atmosphere box "A" and six ocean boxes (Fig. S4a online). The surface ocean (above 200 m) is divided at 45°N/S and contains a southern box "S", an equatorial box "E" and a northern box "N". The deep ocean (200–2500 m) contains a northern deep box "D" and a southern intermediate box "I". The boundary between "D" and "I" is also at 45°S. The bottom-ocean box "B" covers the water-depth range of 2500–4500 m. The flow Q1 represents the Northern Component Water and the flow Q2/Q3 represents the Southern Component Water. They are analogous to the modern ocean circulation. Symbols such as "f_{si}" indicate mixing of water between two adjacent boxes. The volume of each box and the flow rates are listed in Ref. [56].

(ii) Biogeochemical scheme. The main biogeochemical processes in our model are shown in Ref. [56] (Fig. S4b online). The atmosphere box receives tectonic degassing CO_2 with a $\delta^{13}C$ value of −5‰ [57]. Atmospheric CO_2 is further consumed by the weathering of silicate rocks. The initial atmospheric CO_2 is set at 400 ppm. Surface-ocean boxes receive the dissolved inorganic carbon, alkalinity and the nutrient input via chemical weathering of carbonate and silicate rocks. Weathering rates depend on the concentrations of atmospheric CO_2. Primary productivity occurs in the three surface ocean boxes. In this study, we allow the photosynthetic isotope effect (ε_p) of marine algae to vary with the CO_2 concentrations according to [58]

$$25 - \varepsilon_p = \frac{(a \times [PO_4^{3-}]) + 38.39}{[CO_{2(aq)}]}, \quad (2)$$

where a = 0 because riverine phosphate input is almost completely consumed by algae in our model. $[CO_{2(aq)}]$ is the dissolved CO_2 in the surface ocean. Phosphate concentrations control the export of particulate organic carbon, which sinks and remineralizes in the deep and bottom ocean boxes. Only a small fraction of the sinking particulate organic carbon is ultimately sequestered in sediments. In the control experiment (CNTR), the fraction of buried organic carbon in the bottom box is set at 1% of the primary productivity in three surface ocean boxes. Deposition and dissolution of carbonate take place in the equatorial surface and the bottom-ocean boxes. Shallow water carbonate burial in the equatorial box is initially set at 9×10^{12} mol/a and varies along with the ETP (the sum of normalized eccentricity, tilt, and precession in the form of $E + T - P$). Deep water carbonate deposition and dissolution are controlled by the concentrations of carbonate ion ($\left[CO_3^{2-}\right]_B$) in the box "B". When the $\left[CO_3^{2-}\right]_B$ is larger and less than 85 μmol/kg, the burial and the dissolution of calcium carbonate ($CaCO_3$) will take place, respectively.

3. Results

3.1. Benthic stable isotope of U1505C

Benthic $\delta^{18}O$ varies between 0.21‰ and 2.88‰ and shows an overall increasing trend of ~1.07‰ from 21 to 6.25 Ma (Fig. 1a).

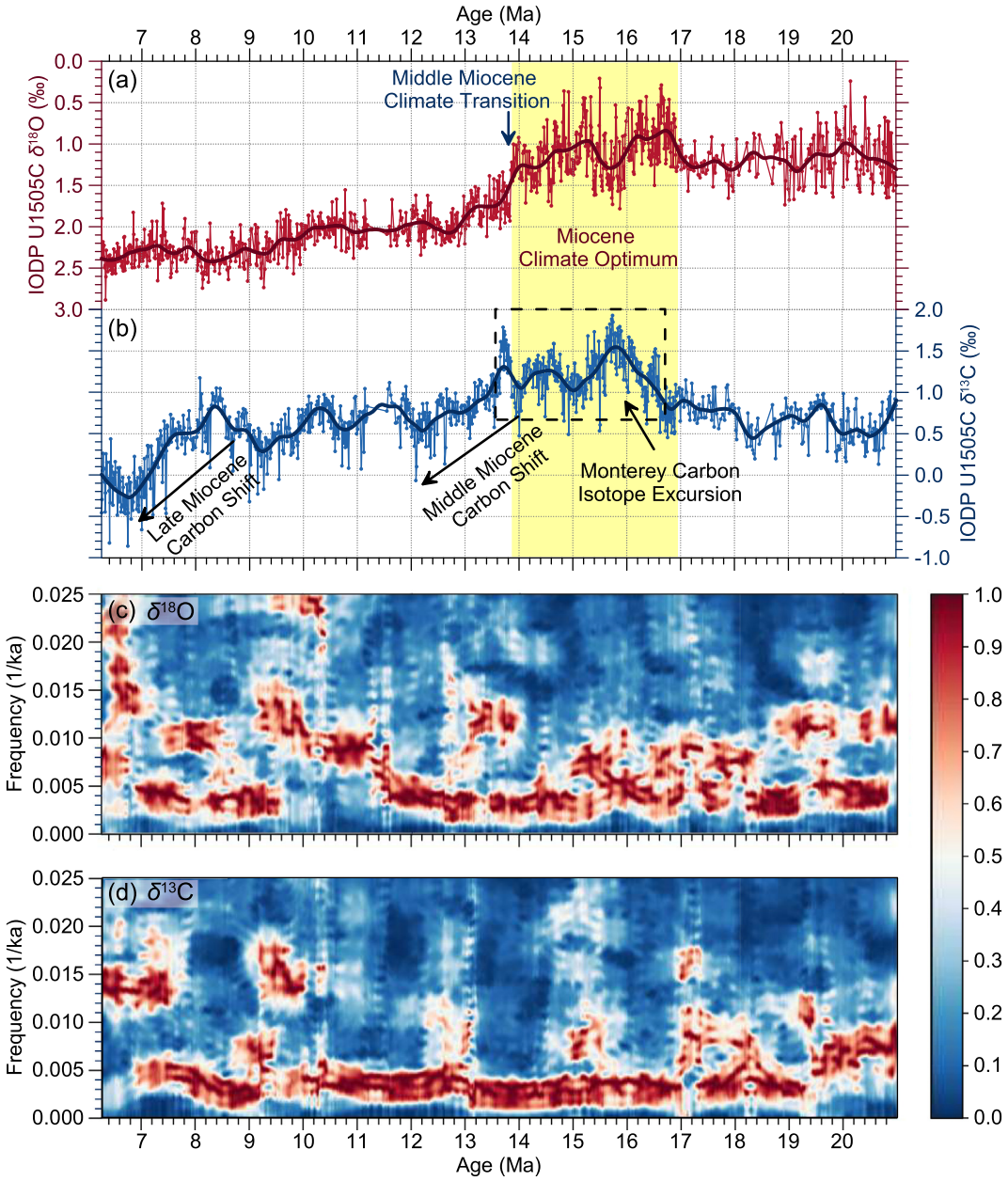

Fig. 1. Temporal trend of isotope records from IODP U1505C. (a) Benthic foraminiferal $\delta^{18}O$. (b) Benthic foraminiferal $\delta^{13}C$. Dark red and blue lines represent the locally weighted regression smooth splines using a 1 Ma window. The black dashed square indicates the Monterey Carbon Isotope Excursion (MCIE), and the yellow shading marks the Miocene Climate Optimum (MCO). Two carbon shift events during the Middle and Late Miocene are indicated by arrows. (c, d) Evolutionary multi-taper spectrogram of benthic $\delta^{18}O$ and $\delta^{13}C$ performed using the Acycle [61]. The spectrograms were calculated with a 1 Ma window on the detrended records of benthic $\delta^{18}O$ and $\delta^{13}C$. Prior to analysis, they were interpolated to evenly spaced sequences with a step of 10 ka.

We divide the evolution of the $\delta^{18}O$ record into three phases. The first phase is between 21 and 16.93 Ma with an average value of ~1.19‰. The amplitude variability is high up to ~1.0‰ until ~18.87 Ma, followed by a relatively small oscillation of ~0.5‰ between ~18.87 and 16.93 Ma. The second phase corresponds to the MCO, starting with an abrupt $\delta^{18}O$ decrease of ~0.8‰ at ~16.96 Ma and ending with a rapid $\delta^{18}O$ increase of ~0.9‰ following the Middle Miocene Climate Transition at ~13.83 Ma [6,18,42]. This phase is characterized by the lowest mean $\delta^{18}O$ value of 1.08‰ and the highest $\delta^{18}O$ amplitude fluctuation of ~1.2‰. Between ~13.83 and 6.25 Ma is the third phase, during which $\delta^{18}O$ oscillates around a mean of 2.13‰ with a small amplitude of ~0.4‰ and shows a stepwise increasing trend of ~0.93‰.

In comparison with the benthic $\delta^{18}O$ record, the $\delta^{13}C$ record shows a different long-term trend and short-term variability throughout 21–6.25 Ma (Fig. 1b). We also divide the evolution of the $\delta^{13}C$ record into three phases. The first phase spans 21–16.68 Ma with an average value of ~0.69‰. The second phase coincides with the MCIE (16.68–13.65 Ma) and is marked by a rapid $\delta^{13}C$ rise of ~1.0‰ at the onset and a relatively high mean value of 1.26‰ [18,19]. The third phase (13.65–6.25 Ma) shows a secular $\delta^{13}C$ decline of 1.28‰, characterized by two episodes of negative $\delta^{13}C$ shifts of ~1.0‰ at the beginning and at the end of this interval. These two $\delta^{13}C$ shift events are referred to as the Middle (13.65–12.09 Ma) and the Late (7.48–6.68 Ma) Miocene Carbon Shift, respectively [44,48–50]. Taken together, the temporal

patterns of benthic stable isotope from IODP U1505C are highly similar to those from the open Pacific and Atlantic Oceans [6,17–19,30,34,40–47,49,50,59,60]. Additionally, both benthic $\delta^{18}O$ and $\delta^{13}C$ records contain prominent 405-ka cycles, but only the $\delta^{18}O$ series shows pronounced variations at the 100-ka cycle during most periods of 21–6.25 Ma (Fig. 1c, d).

3.2. Time evolutive phase relationship between $\delta^{18}O$ and $\delta^{13}C$

We compiled a total of nine high-resolution benthic foraminiferal $\delta^{18}O$ and $\delta^{13}C$ records from the 34–6 Ma time interval, using their astronomically-tuned age models [6,17–19,24,30,31,34,40–47,49,50,59,60,62] (Fig. 2, Figs. S5–S13 and Table S1 online). The selected $\delta^{18}O$ and $\delta^{13}C$ data were all derived from *Cibicidoides wuellerstorfi* and/or *Cibicidoides mundulus*. These parallel benthic $\delta^{18}O$ and $\delta^{13}C$ sequences show strong and in-phase interactions on the 405-ka eccentricity timescales throughout the Oligo-mid Miocene (~34–12 Ma) (Fig. 2h and Figs. S5–S15 online). Between ~12 and 6 Ma, the $\delta^{18}O$-$\delta^{13}C$ coherence in the 405-ka bands is relatively weak in many cores due to the obscuration of the 405-ka cycle in benthic $\delta^{18}O$ series (Figs. S5–S7 online).

The evolutive phase analysis reveals that changes in $\delta^{18}O$ slightly lead those of $\delta^{13}C$ by an average of ~19.2 ka at the 405-ka cycle during most of the Oligo-Miocene (Fig. 2h and Fig. S14c online). However, the period between ~16.9 and 14.7 Ma stands out as an exception, characterized by a $\delta^{18}O$-$\delta^{13}C$ phase shift at the 405-ka cycle. Reconstructed data from four sites (ODP 1146, IODP U1337, U1338 and U1505) cover this interval, and they all show that benthic $\delta^{13}C$ leads $\delta^{18}O$ by a mean of ~17.0 ka in the 405-ka bands (Fig. 2h and Fig. S14b online). At IODP U1505C, when employing the minimum tuning age model and conducting a repeated analysis of the evolutive phase analysis, the $\delta^{13}C$-lead-$\delta^{18}O$ phenomenon remains (Fig. S16 online). This suggests that this phase shift is not sensitive to the astronomical tuning methods. This distinct $\delta^{13}C$-lead-$\delta^{18}O$ period overlaps with the MCO and large-scale tectonic CO_2 emissions (Fig. 2d, e). It is noteworthy that we do not observe an unambiguous $\delta^{13}C$-lead-$\delta^{18}O$ in the 100-ka bands during the MCO, probably due to the obscuration of the 100-ka cycle in $\delta^{13}C$ records during this period (Fig. 1d and Figs. S5d–S8d online).

In addition, two other periods with the $\delta^{13}C$-lead-$\delta^{18}O$ phenomenon are also found in reconstructed data from two ODP sites (Fig. 2h and Fig. S14 online), one between 10.80 and 10.60 Ma corresponding to the Tortonian Thermal Maximum (ODP 1146) (Fig. S6 online) [44] and the other between 21.14 and 20.54 Ma (ODP 1090) (Fig. S9 online) [59]. However, the presence of these two exceptional periods is not supported by other IODP/ODP sites (ODP Sites 926, 929, 1218, 1264 and IODP Sites U1337, U1505) (Figs. S5, S7, and S10–S13 online) [6,24,30,31,40,41,46,49,50,60,62], which casts doubt on their global extent. Therefore, we focus only on the $\delta^{13}C$-lead-$\delta^{18}O$ signal during the MCO.

3.3. Sensitivity of $\delta^{18}O$ and $\delta^{13}C$ to eccentricity forcing

We calculated the sensitivity of benthic $\delta^{18}O$ (S_{ecc}-$\delta^{18}O$) and $\delta^{13}C$ (S_{ecc}-$\delta^{13}C$) to eccentricity forcing at the 405-ka cycle (Fig. 2f, g). S_{ecc}-$\delta^{18}O$ and S_{ecc}-$\delta^{13}C$ are relatively low during the Oligocene (~34–24.5 Ma), with an average value of 0.020×10^{-6} and 0.034×10^{-6}, respectively. They apparently increase between 24.5 and 13 Ma, featured by several high peaks up to $\sim0.1\times10^{-6}$–0.3×10^{-6}. Thereafter, S_{ecc}-$\delta^{18}O$ decreases to low values. In contrast, S_{ecc}-$\delta^{13}C$ remains relatively high over ~13–6 Ma.

3.4. Simulation of marine $\delta^{13}C$ variations at the eccentricity cycles

The CNTR experiment was spun at a fixed carbon degassing rate of 7.78×10^{12} mol/a with a $\delta^{13}C$ value of −5.0‰ [57] and forced by the ETP [63] between 17 and 13 Ma (Fig. 3). On the basis of the CNTR run, three additional sensitivity tests were designed. In the first scenario (SCEN1), we varied the tectonic CO_2 degassing rate to the atmosphere box, based on the changing CRBG emplacement and seafloor spreading rates. The timing and amount of carbon emissions were taken from existing studies [8,11,15] (Fig. 3a and Table S5 online). In the second scenario (SCEN2), the fraction of buried organic carbon relative to the settling organic matter was made variable, assuming that more deep-sourced carbon entering the atmosphere would result in broader flooding of continental shelves, enhancing the burial of organic carbon. This fraction was arbitrarily set between 0.75% and 3% (Fig. 3b and Table S6 online). In the third integrated experiment (INT), we adopted both forcings used in the SCEN1 and SCEN2 (Fig. 3c).

In the control experiment (Fig. 3), both simulated atmospheric pCO_2 and $\delta^{13}C_{CNTR}$ of dissolved inorganic carbon in the deep ocean show strong variance in the 405-ka bands between 17 and 13 Ma, following the temporal pattern of the ETP. Compared to the CNTR (Fig. 3a), the relatively high deep-sourced carbon input in the SCEN1 experiment during 16.7–14.9 Ma elevates the mean pCO_2 level by ~137 ppm and causes a more depleted $\delta^{13}C_{SCEN1}$ by ~0.4‰. Between 14.9 and 13 Ma, when the tectonic CO_2 degassing rate falls below the background level, the mean pCO_2 is ~106 ppm lower and the mean $\delta^{13}C_{SCEN1}$ is ~0.6‰ more positive than the CNTR results. The evolutive phase analysis suggests that $\delta^{13}C_{SCEN1}$ leads $\delta^{13}C_{CNTR}$ by an average of 3.1 ka in the 405-ka bands during 16.7–14.9 Ma. This phase offset shifts to nearly zero during 14.9–13 Ma, along with a reduced effect of the carbon injection.

In the SCEN2 experiment (Fig. 3b), changes in the fraction of organic carbon burial have a negligible effect on the atmospheric pCO_2, which could be attributed to the buffering effect of ocean alkalinity. A higher organic burial rate corresponds to a decrease of ocean alkalinity and a lower capacity to sequester dissolved CO_2 in the ocean (Fig. S17 online). Conversely, the higher organic carbon burial during 17–13.8 Ma results in a significantly more positive excursion of $\delta^{13}C_{SCEN2}$ than $\delta^{13}C_{CNTR}$, with an average shift of ~0.66‰. Moreover, $\delta^{13}C_{SCEN2}$ leads $\delta^{13}C_{CNTR}$ by an average of ~6.9 ka at the 405-ka cycle.

In the INT experiment (Fig. 3c), atmospheric pCO_2 are determined by the tectonic degassing rates, thus showing a similar pattern to the SCEN1 result. The effect of isotopically depleted carbon input seems to be counterbalanced by enhanced organic carbon burial between 17 and 14.9 Ma, giving rise to a moderate change in $\delta^{13}C_{INT}$ compared to $\delta^{13}C_{CNTR}$. However, increases in both the tectonic degassing rates and organic carbon burial combine to cause an apparent $\delta^{13}C_{INT}$-lead-$\delta^{13}C_{CNTR}$ phenomenon in the 405-ka bands, with an average lead of 12.1 ka between 17 and 14.9 Ma.

4. Discussion

4.1. The mysterious Monterey carbon isotope excursion

The ~1.0‰ positive excursion in global ocean $\delta^{13}C$ during ~16.7–13.6 Ma (Figs. 1b, 2c and Figs. S5b–S8b online) has long been a mystery [4,8,19,21,23]. Recent advances have further complicated the mechanism of the MCIE. First, current estimates of tectonic degassing rates during the MCO, sourced from the CRBG emplacement and ocean crustal production, are considerably higher than previously thought [8,11,15]. This deep-sourced carbon is assumed to have a light isotope value of −5‰ [57], which

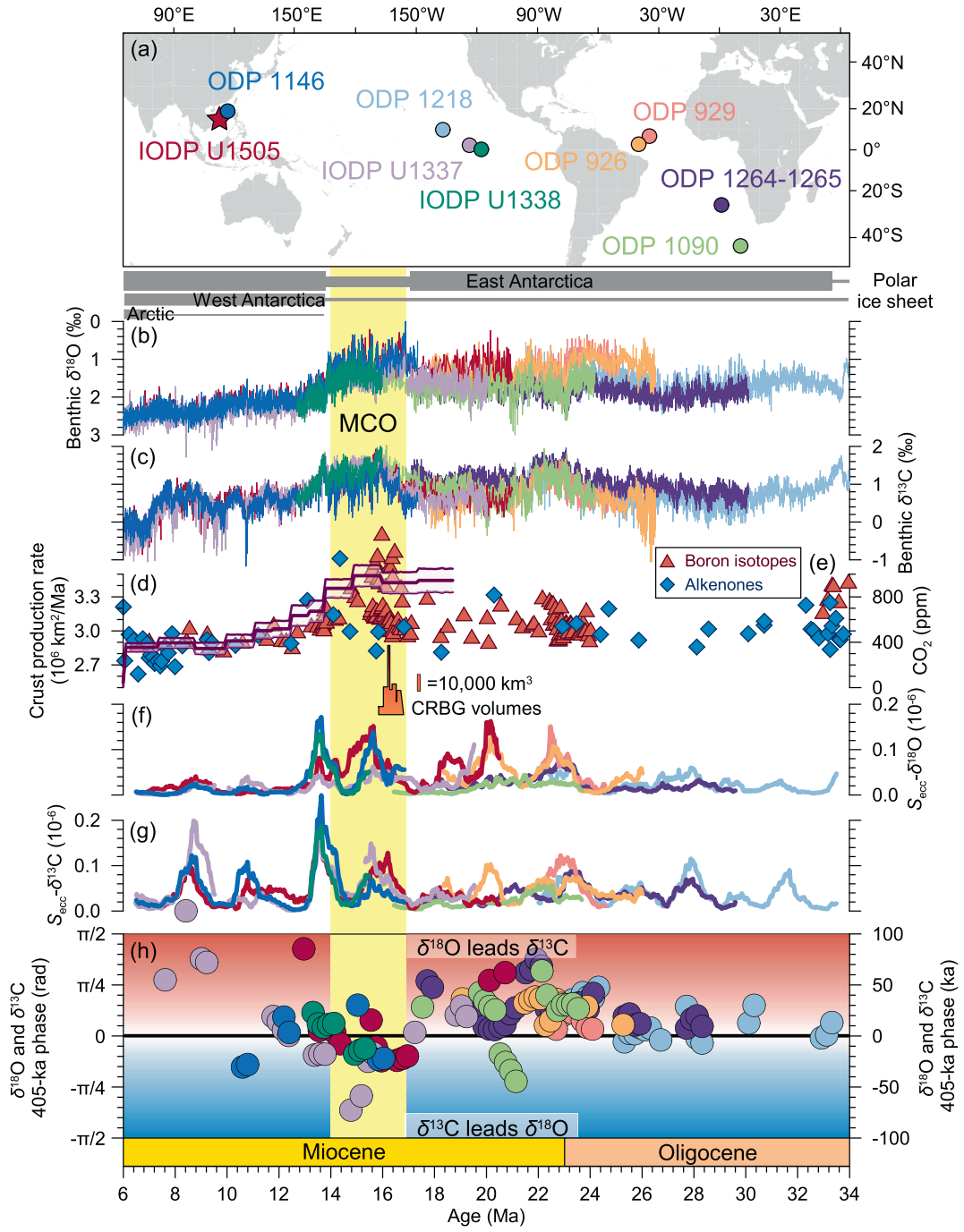

Fig. 2. Evolutive phase relationship between benthic $\delta^{18}O$ and $\delta^{13}C$ records at the 405-ka cycle during the Oligo-Miocene. (a) Locations of the sites discussed in this study [6,17–19,24,30,31,34,40–47,49,50,59,60,62], highlighting the new IODP Site U1505 (red star). (b, c) Overview of the benthic $\delta^{18}O$ and $\delta^{13}C$ records with the evolution of the polar ice sheets (gray shadow) [6]. (d) Global ocean crust production rates (purple curve) with 95% confidence intervals [15]. (e) Reconstructed atmospheric CO_2 levels derived from boron isotope (red triangle) and alkenone (blue square) [2]. The occurrence of the Columbia River Basalt Group (CRBG) is shown by an orange rectangle [8,11] (f, g) Eccentricity sensitivity of benthic $\delta^{18}O$ and $\delta^{13}C$ (S_{ecc}-$\delta^{18}O$ and S_{ecc}-$\delta^{13}C$) from selected IODP/ODP sites. (h) Evolutive phase relationship between $\delta^{18}O$ and $\delta^{13}C$ records in the 405-ka bands. Only results with a coherence >0.6 are presented. Positive and negative phase relationships indicate that $\delta^{18}O$ leads and lags $\delta^{13}C$, respectively. Yellow shading marks the period when $\delta^{13}C$ leads $\delta^{18}O$ during the MCO.

is much more negative than the $\delta^{13}C$ of marine inorganic carbon. Second, the mid-Miocene is the period with the lowest organic carbon accumulation rate in the global deep ocean throughout the Neogene, as warm seawater is inferred to stimulate the temperature-dependent microbial degradation of organic matter [64]. Both processes should have caused a negative excursion rather than a positive shift in marine $\delta^{13}C$.

Initially, the Monterey Hypothesis was proposed that invigorated coastal upwelling has led to marine algal blooms and organic carbon burial in the circum-Pacific Ocean, eventually causing the positive $\delta^{13}C$ shift in global ocean [23]. This explanation is partly supported by the widespread deposition of the oil-rich Monterey Formation along the Californian coast [21,65]. Indeed, ocean margins could serve as critical organic carbon reservoirs under warmer climatic conditions [22], given that modern continental shelves contribute ~80% of organic carbon burial in sediments [66]. Furthermore, peat/lignite was extensively deposited both on land and on the drowning continental shelves during the MCO, due to

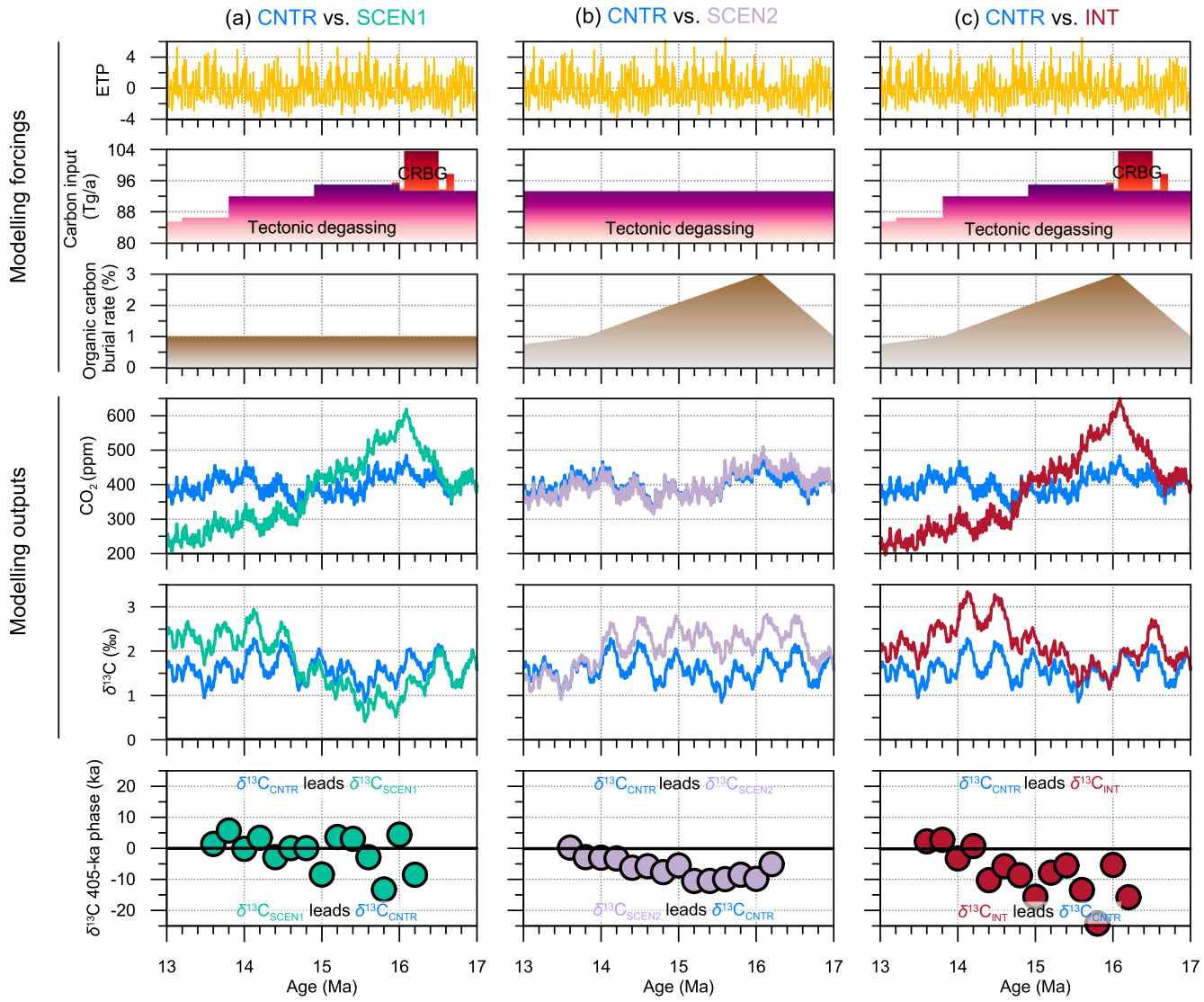

Fig. 3. Comparison of simulation results in different experiments. Comparison between the CNTR and the SCEN1 (a), the CNTR and the SCEN2 (b), and the CNTR and the INT (c). Modelling forcings include changes in the ETP, the tectonic degassing carbon input (Tg = 10^{12} g), and the fraction of buried organic carbon. Model outputs presented here are atmospheric CO_2 concentrations and the $\delta^{13}C$ of dissolved inorganic carbon in bottom waters. The evolutive phase relationship between the $\delta^{13}C_{CNTR}$ and the $\delta^{13}C_{SCEN1/SCEN2/INT}$ at the 405-ka cycle is shown.

higher temperatures and enhanced low-latitude hydrological cycle [4,67,68]. Thus, despite the opposite role of deep seas, there may still have been an overall increase in organic carbon sequestration on a global scale during the MCO.

Since our box model does not include the terrestrial carbon reservoir and the process of organic matter burial in shallow seas (Fig. S4 online), we increased the seafloor organic carbon sequestration as an approximate approach to simulate the growth of organic carbon deposition over the globe. In the model, an increase in fraction of buried organic matter from 1% to 2%–3% can effectively enrich the $\delta^{13}C$ of ocean inorganic carbon pool (Fig. 3b). However, this remains insufficient to overcompensate for the effect of massive carbon emissions between 16.7 and 14.9 Ma, and our experiment is unable to generate a 1.0‰ positive excursion in marine $\delta^{13}C$ (Fig. 3c).

Another suggestion is that strengthened $\delta^{13}C$ fractionation during photosynthesis in marine algae at high CO_2 levels may facilitate the transfer of more ^{12}C from the atmosphere–ocean system into buried organic matter [8,58]. In our model, the photosynthetic $\delta^{13}C$ fractionation of marine algae was set variable and changed with atmospheric pCO_2. However, comparing the results between CNTR and SCEN1 experiments, the mean $\delta^{13}C_{SCEN1}$ is still ~0.40‰ depleted than the $\delta^{13}C_{CNTR}$ during 16.7–14.9 Ma (Fig. 3a). This indicates that the photosynthetic isotope effect alone is not enough to drive the long-lived MCIE, either.

Therefore, additional light carbon reservoirs are required to store ^{12}C from the atmosphere and the marine inorganic carbon pool. The dissolved organic carbon reservoir in the ocean may play such a role. The substantial increase in remineralization of particulate organic matter and the stimulation of microbial activity during the MCO [64] may have contributed to the expansion of the dissolved organic carbon reservoir [69], which could promote ^{12}C sequestration. This idea needs to be tested by biogeochemical models that include the marine dissolved organic carbon module.

4.2. Carbonate deposition shift accounts for synchronized climate-carbon cycle

The long-lasting MCIE was superimposed by eight $\delta^{13}C$ maxima events, which co-varied with $\delta^{18}O$ on the 405-ka eccentricity timescale [19,21]. Such in-phase $\delta^{18}O$-$\delta^{13}C$ behavior has been observed throughout the Oligo-Miocene [6,17–19,24,30,31,34,40–47,49,50,

59,60,62] (Fig. 2h and Figs. S5–S15 online) and attributed to the control of eccentricity on both Antarctic ice volume and net carbon transfer between the land biosphere and the ocean [17].

Here, we propose that shifts in the center of carbonate deposition between pelagic environments and shallower waters may also contribute to this in-phase phenomenon [56,70]. Eccentricity maxima (Fig. 4a) have resulted in warmer climatic conditions and shrinkage of the Antarctic cryosphere, leading to sea-level rise and a decrease in seawater $\delta^{18}O$. Simultaneously, strong monsoon rainfall and chemical weathering at low latitudes could transport more alkalinity and nutrients into the ocean. The increased alkalinity input is inferred to cause massive carbonate accumulation on the submerged continental shelves, sequestering isotopically heavy carbon (^{13}C) in shallow-sea sediments and dropping deep-sea $\delta^{13}C$. Model results also show that a rise of 30 $\times$ 10^{12} mol/a in shallow-sea calcium carbonate burial coincides with a reduction of ~30 μmol/kg in deep-sea carbonate ion concentrations, alongside a decrease of ~1‰ in the deep sea $\delta^{13}C$ (Fig. S18 online) [56]. Conversely, the opposite processes have occurred during periods of eccentricity minima (Fig. 4b).

Overall, eccentricity-driven variations of benthic $\delta^{18}O$ and $\delta^{13}C$ during the Oligo-Miocene were two independent processes. The former was related to ice-volume fluctuations in the southern high latitudes, and the latter was determined by the low-latitude hydrological cycle. This is in sharp contrast to the scenario during the Plio-Pleistocene, when benthic $\delta^{18}O$-$\delta^{13}C$ interactions were anti-phase at the 405-ka cycle, and both were controlled by high-latitude climate processes [17]. Consequently, tropical climate processes played a dominant role in regulating the marine carbon cycle when Earth's climate was in a warm state during the Oligo-Miocene.

4.3. Accelerated marine carbon cycle during the MCO

Although their overall interactions are in-phase throughout the Oligo-Miocene, an average lag of benthic $\delta^{13}C$ relative to $\delta^{18}O$ of ~17.0 ka is found at the 405-ka cycle (Fig. 2h, Figs. S5e–S13e and S14c online). This phase lag has been explained by the ~65 ka residence time of carbon in the ocean [17,24,30,31]. In this study, we unravel an observation of $\delta^{13}C$-lead-$\delta^{18}O$ in the 405-ka bands during the MCO (Figs. 2h (yellow shadow) and 4c and Figs. S14b online), suggesting that the response of marine carbon cycle to the eccentricity forcing is accelerated and becomes faster than that of the climate-cryosphere system. Previously, De Vleeschouwer et al. [17] found a $\delta^{13}C$-lead-$\delta^{18}O$ phase relationship in the 100-ka bands during the Miocene, when precession amplitudes exceeded a certain threshold due to the modulation of the 2.4-Ma cycle. However, their explanation probably cannot be applied to the $\delta^{13}C$-lead-$\delta^{18}O$ phenomenon at the 405-ka cycle, because the amplitude of the 405-ka cycle is only weakly modulated by the 2.4-Ma cycle (Fig. S19 online) [63].

Supported by both marine and terrestrial proxies, the MCO represents one of the strongest monsoon periods across the entire Miocene (Fig. S20 online) [32–36,44,71–75]. However, a further analysis of the phase relationship between monsoon precipitation indicators and the 405-ka eccentricity cycle is impeded by the current scarcity of high-resolution data. At the same time, while the deep ocean plays an opposing role [64], a potential global net rise in organic carbon burial during the MCO remains plausible [4,66–68]. Our model results suggest that the elevation of weathering fluxes concerning silicates and carbonates, associated with an augmentation in organic carbon burial, can shorten the residence time of carbon in the deep-sea reservoir (Fig. 3 and Fig. S21 online). Furthermore, the higher S_{ecc}-$\delta^{13}C$ since the onset of MCO indicates that the oceanic carbon cycle is more sensitive to the 405-ka eccentricity forcing (Fig. 2g). Taken together, we propose that enhanced

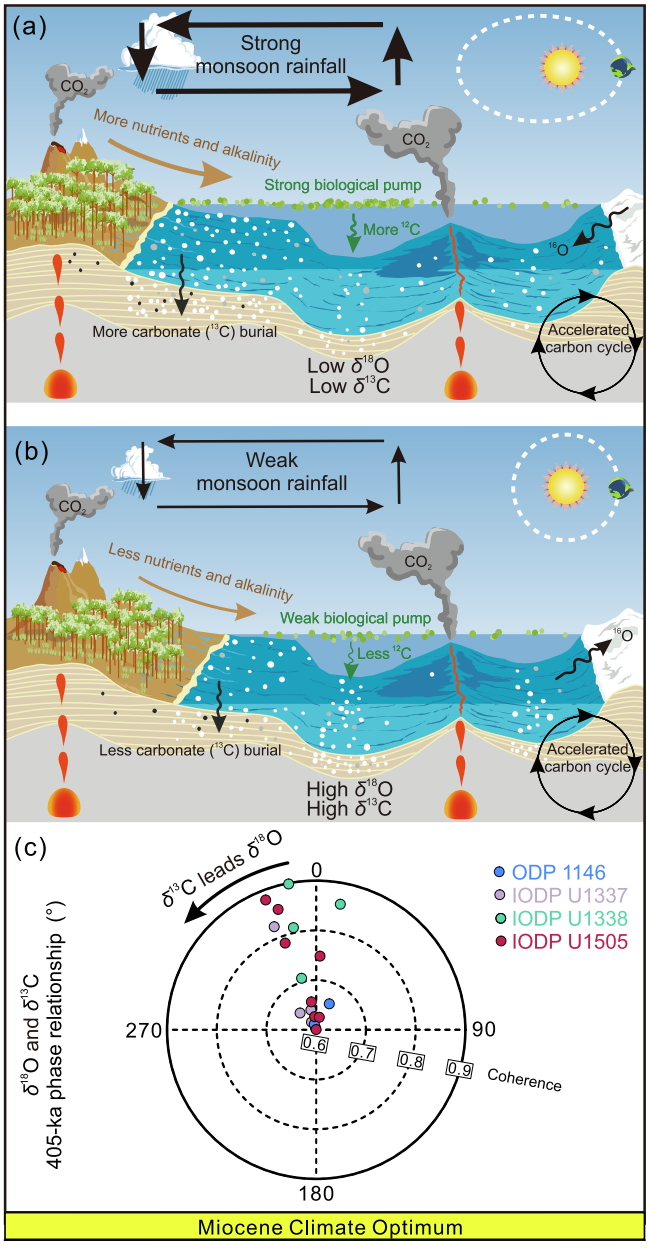

Fig. 4. Cartoons illustrating the mechanisms for $\delta^{13}C$-lead-$\delta^{18}O$ at the 405-ka cycle during the MCO. (a) Eccentricity maxima can cause a shrinkage of the Antarctic ice volume and an increased ^{16}O (isotopically light oxygen) transfer to the ocean. Simultaneously, enhanced monsoons and continental weathering can transport more alkalinity and nutrients to the ocean, releasing more ^{12}C-enriched carbon into the deep sea. (b) During eccentricity minima, the opposite processes occur. Therefore, benthic $\delta^{18}O$-$\delta^{13}C$ interactions are nearly in phase at eccentricity cycles. (c) Cross-spectral coherence and phase angles between parallel $\delta^{18}O$ and $\delta^{13}C$ records from IODP/ODP Sites 1146 [6,17,19,34,42–44], U1337 [6,18,40,45,49,50], U1338 [6,45,47] and U1505 for the MCO interval, and they show that variations of benthic $\delta^{13}C$ lead those of $\delta^{18}O$ in the 405-ka bands. In general, the relatively long residence time of carbon in the deep ocean facilitates a lead of benthic $\delta^{18}O$ relative to $\delta^{13}C$. The MCO greenhouse effect is likely to have accelerated the response of marine carbon cycle to eccentricity forcing, generating the $\delta^{13}C$-lead-$\delta^{18}O$ scenario.

chemical weathering triggers faster propagation of ^{12}C-enriched carbon from the atmosphere to the ocean, while increased photosynthetic $\delta^{13}C$ fractionation in marine algae and organic carbon burial accelerates the ^{12}C removal from the ocean (Fig. 4). Additionally, more riverine alkalinity input to the ocean leads to massive carbonate accumulation along the continental margins,

speeding up the transfer of ^{13}C from seawater to sediments (Fig. 4). Ultimately, these low-latitude climate processes give rise to a moderate but explicit phase shift between benthic $\delta^{18}O$ and $\delta^{13}C$ at the 405-ka cycle during the MCO (Figs. 2h (yellow shadow), 4c and Fig. S14b online). Since our model does not account for ice-sheet processes and oxygen isotope (Fig. S4 online), we cannot directly test changes in the phase relationship between $\delta^{18}O$ and $\delta^{13}C$. In the future, isotope-enabled general circulation models, coupled with a dynamic Antarctic volume and carbon-cycle, are needed to test our hypothesis.

Conflict of interest

The authors declare that they have no conflict of interest.

Acknowledgments

This work was supported by the National Natural Science Foundation of China (42122042, 42030403, and 42188102), the Fundamental Research Funds for the Central Universities (22120220531), the Shanghai Pilot Program for Basic Research, and the Netherlands Earth System Science Centre (024.002.001). We thank Xiaoying Jiang (Tongji University) for laboratory assistance, Jiawang Wu (Sun Yat-sen University) for thoughtful comments, and the Integrated Ocean Discovery Program (IODP) for providing samples.

Author contributions

Fenghao Liu, Enqing Huang, and Jun Tian designed research; Fenghao Liu and Enqing Huang performed research; Jinlong Du and Wentao Ma ran simulation; Fenghao Liu, Enqing Huang, and Xiaolin Ma analyzed data; Fenghao Liu and Enqing Huang wrote the paper with contributions from Lucas J. Lourens and Jun Tian.

Appendix A. Supplementary materials

Supplementary materials to this article can be found online at https://doi.org/10.1016/j.scib.2023.12.052.

References

[1] Foster GL, Lear CH, Rae JWB. The evolution of pCO_2, ice volume and climate during the middle Miocene. Earth Planet Sci Lett 2012;341–344:243–54.
[2] Rae JWB, Zhang YG, Liu X, et al. Atmospheric CO_2 over the past 66 million years from marine archives. Annu Rev Earth Planet Sci 2021;49:609–41.
[3] Sosdian SM, Greenop R, Hain MP, et al. Constraining the evolution of Neogene ocean carbonate chemistry using the boron isotope pH proxy. Earth Planet Sci Lett 2018;498:362–76.
[4] Sosdian SM, Babila TL, Greenop R, et al. Ocean carbon storage across the middle Miocene: A new interpretation for the Monterey Event. Nat Commun 2020;11:134.
[5] Steinthorsdottir M, Coxall HK, de Boer AM, et al. The Miocene: The future of the past. Paleoceanogr Paleoclimatol 2021;36:e2020PA004037.
[6] Westerhold T, Marwan N, Drury AJ, et al. An astronomically dated record of Earth's climate and its predictability over the last 66 million years. Science 2020;369:1383–7.
[7] You Y, Huber M, Müller RD, et al. Simulation of the Middle Miocene Climate Optimum. Geophys Res Lett 2009;36:L04702.
[8] Armstrong MKay DI, Tyrrell T, Wilson PA, et al. Estimating the impact of the cryptic degassing of Large Igneous Provinces: A mid-Miocene case-study. Earth Planet Sci Lett 2014;403:254–62.
[9] Barry TL, Kelley SP, Reidel SP, et al. Eruption chronology of the Columbia River Basalt Group. In: Reidel SP, Camp VE, Ross ME, editors. The Columbia River Flood Basalt Province, 497. Boulder: The Geological Society of America; 2013. p. 45–66.
[10] Friedlingstein P, O'Sullivan M, Jones MW, et al. Global carbon budget 2022. Earth Syst Sci Data 2022;14:4811–900.
[11] Kasbohm J, Schoene B. Rapid eruption of the Columbia River flood basalt and correlation with the mid-Miocene climate optimum. Sci Adv 2018;4:eaat8223.
[12] Longman J, Mills BJW, Donnadieu Y, et al. Assessing volcanic controls on Miocene climate change. Geophys Res Lett 2022;49:e2021GL096519.
[13] Reidel S. The Columbia River Basalt Group: A flood basalt province in the Pacific Northwest, USA. Geosci Can 2015;42:151–68.
[14] Tian X, Buck WR. Intrusions induce global warming before continental flood basalt volcanism. Nat Geosci 2022;15:417–22.
[15] Herbert TD, Dalton CA, Liu Z, et al. Tectonic degassing drove global temperature trends since 20 Ma. Science 2022;377:116–9.
[16] De Vleeschouwer D, Vahlenkamp M, Crucifix M, et al. Alternating Southern and Northern Hemisphere climate response to astronomical forcing during the past 35 m.y. Geology 2017;45:375–8.
[17] De Vleeschouwer D, Drury AJ, Vahlenkamp M, et al. High-latitude biomes and rock weathering mediate climate–carbon cycle feedbacks on eccentricity timescales. Nat Commun 2020;11:5013.
[18] Holbourn A, Kuhnt W, Kochhann KGD, et al. Global perturbation of the carbon cycle at the onset of the Miocene Climatic Optimum. Geology 2015;43:123–6.
[19] Holbourn A, Kuhnt W, Schulz M, et al. Orbitally-paced climate evolution during the middle Miocene "Monterey" carbon-isotope excursion. Earth Planet Sci Lett 2007;261:534–50.
[20] Tian J, Ma W, Lyle MW, et al. Synchronous mid-Miocene upper and deep oceanic $\delta^{13}C$ changes in the east equatorial Pacific linked to ocean cooling and ice sheet expansion. Earth Planet Sci Lett 2014;406:72–80.
[21] Woodruff F, Savin SM. $\delta^{13}C$ values of Miocene Pacific benthic foraminifera: Correlations with sea level and biological productivity. Geology 1985;13:119–22.
[22] Ma P, Liu Z, Jiang M, et al. Carbon sequestration of the middle Miocene Sunda Shelf facilitated global climate change. Geophys Res Lett 2022;49: e2022GL100638.
[23] Vincent E, Berger WH. Carbon dioxide and polar cooling in the Miocene: The Monterey hypothesis. In: Sundquist E, Broecker W, editors. The Carbon Cycle and Atmospheric CO_2: Natural Variations Archean to Present, 32. Washington DC: American Geophysical Union; 1985. p. 455–468.
[24] Pälike H, Norris RD, Herrle JO, et al. The heartbeat of the oligocene climate system. Science 2006;314:1894–8.
[25] de Boer B, Lourens LJ, van de Wal RSW, et al. Persistent 400,000-year variability of Antarctic ice volume and the carbon cycle is revealed throughout the Plio-Pleistocene. Nat Commun 2014;5:2999.
[26] Lisiecki LE, Raymo ME. A Pliocene-Pleistocene stack of 57 globally distributed benthic $\delta^{18}O$ records. Paleoceanography 2005;20:PA1003.
[27] Turner SK. Pliocene switch in orbital-scale carbon cycle/climate dynamics. Paleoceanography 2014;29:1256–66.
[28] Herbert TD, Lawrence KT, Tzanova A, et al. Late Miocene global cooling and the rise of modern ecosystems. Nat Geosci 2016;9:843–7.
[29] Cao M, Wang Z, Sui Y, et al. Mineral dust coupled with climate-carbon cycle on orbital timescales over the past 4 Ma. Geophys Res Lett 2021;48: e2021GL095327.
[30] Liebrand D, Beddow HM, Lourens LJ, et al. Cyclostratigraphy and eccentricity tuning of the early Oligocene through early Miocene (30.1–17.1 Ma): Cibicides mundulus stable oxygen and carbon isotope records from Walvis Ridge Site 1264. Earth Planet Sci Lett 2016;450:392–405.
[31] Zachos JC, Shackleton NJ, Revenaugh JS, et al. Climate response to orbital forcing across the Oligocene-Miocene boundary. Science 2001;292:274–8.
[32] Clift PD, Wan S, Blusztajn J. Reconstructing chemical weathering, physical erosion and monsoon intensity since 25 Ma in the northern South China Sea: A review of competing proxies. Earth Sci Rev 2014;130:86–102.
[33] Clift PD, Betzler C, Clemens SC, et al. A synthesis of monsoon exploration in the Asian marginal seas. Sci Drill 2022;31:1–29.
[34] Holbourn A, Kuhnt W, Clemens SC, et al. A ~12 Myr miocene record of east Asian monsoon variability from the South China Sea. Paleoceanogr Paleoclimatol 2021;36:e2021PA004267.
[35] Ren X, Nie J, Saylor JE, et al. Temperature control on silicate weathering intensity and evolution of the Neogene east Asian Summer Monsoon. Geophys Res Lett 2020;47:e2020GL088808.
[36] Wu F, Fang X, Yang Y, et al. Reorganization of Asian climate in relation to Tibetan Plateau uplift. Nat Rev Earth Environ 2022;3:684–700.
[37] Jian Z, Larsen HC, Zarikian CAA, et al. Site U1505. In: Sun Z, Jian Z, Stock JM, et al., editors. South China Sea Rifted Margin. Proceedings of the International Ocean Discovery Program Volume 367/368, 2018; https://doi.org/10.14379/iodp.proc.367368.109.2018
[38] Holbourn A, Kuhnt W, Simo (Toni) JA, et al. Middle Miocene isotope stratigraphy and paleoceanographic evolution of the northwest and southwest Australian margins (Wombat Plateau and Great Australian Bight). Palaeogeogr Palaeoclimatol Palaeoecol 2004;208:1–22.
[39] Tian J, Zhao Q, Wang P, et al. Astronomically modulated Neogene sediment records from the South China Sea. Paleoceanography 2008;23:PA3210.
[40] Tian J, Yang M, Lyle MW, et al. Obliquity and long eccentricity pacing of the Middle Miocene climate transition. Geochem Geophys Geosyst 2013;14:1740–55.
[41] Drury AJ, Liebrand D, Westerhold T, et al. Climate, cryosphere and carbon cycle controls on Southeast Atlantic orbital-scale carbonate deposition since the Oligocene (30–0 Ma). Clim Past 2021;17:2091–117.
[42] Holbourn A, Kuhnt W, Schulz M, et al. Impacts of orbital forcing and atmospheric carbon dioxide on Miocene ice-sheet expansion. Nature 2005;438:483–7.
[43] Holbourn A, Kuhnt W, Frank M, et al. Changes in Pacific Ocean circulation following the Miocene onset of permanent Antarctic ice cover. Earth Planet Sci Lett 2013;365:38–50.

[44] Holbourn AE, Kuhnt W, Clemens SC, et al. Late Miocene climate cooling and intensification of southeast Asian winter monsoon. Nat Commun 2018;9:1584.
[45] Kochhann KGD, Holbourn A, Kuhnt W, et al. Eccentricity pacing of eastern equatorial Pacific carbonate dissolution cycles during the Miocene Climatic Optimum. Paleoceanography 2016;31:1176–92.
[46] Liebrand D, Lourens LJ, Hodell DA, et al. Antarctic ice sheet and oceanographic response to eccentricity forcing during the early Miocene. Clim Past 2011;7:869–80.
[47] Holbourn A, Kuhnt W, Lyle M, et al. Middle Miocene climate cooling linked to intensification of eastern equatorial Pacific upwelling. Geology 2014;42:19–22.
[48] Drury AJ, John CM, Shevenell AE, et al. Evaluating climatic response to external radiative forcing during the late Miocene to early Pliocene: New perspectives from eastern equatorial Pacific (IODP U1338) and North Atlantic (ODP 982) locations. Paleoceanography 2016;31:167–84.
[49] Drury AJ, Westerhold T, Frederichs T, et al. Late Miocene climate and time scale reconciliation: Accurate orbital calibration from a deep-sea perspective. Earth Planet Sci Lett 2017;475:254–66.
[50] Tian J, Ma X, Zhou J, et al. Paleoceanography of the east equatorial Pacific over the past 16 Myr and Pacific-Atlantic comparison: High resolution benthic foraminiferal $\delta^{18}O$ and $\delta^{13}C$ records at IODP Site U1337. Earth Planet Sci Lett 2018;499:185–96.
[51] Kotov S, Pälike H. QAnalySeries—A cross-platform time series tuning and analysis tool. AGU Fall Meeting Abstract 2018.
[52] Paillard D, Labeyrie L, Yiou P. Macintosh Program performs time-series analysis. Eos Trans AGU 1996;77:379.
[53] Callahan J, Casey R, Sharer G, et al. Classes and methods for seismic data analysis. 2022, https://cran.r-project.org/web/packages/IRISSeismic/index.html.
[54] R Core Team. A language and environment for statistical computing. R Foundation for Statistical Computing. 2013, https://www.r-project.org/.
[55] Levy RH, Meyers SR, Naish TR, et al. Antarctic ice-sheet sensitivity to obliquity forcing enhanced through ocean connections. Nat Geosci 2019;12:132–7.
[56] Ma W, Tian J, Li Q, et al. Simulation of long eccentricity (400-kyr) cycle in ocean carbon reservoir during Miocene Climate Optimum: Weathering and nutrient response to orbital change. Geophys Res Lett 2011;38:L10701.
[57] Deines P. The carbon isotope geochemistry of mantle xenoliths. Earth Sci Rev 2002;58:247–78.
[58] Kump LR, Arthur MA. Interpreting carbon-isotope excursions: Carbonates and organic matter. Chem Geol 1999;161:181–98.
[59] Billups K, Pälike H, Channell JET, et al. Astronomic calibration of the late Oligocene through early Miocene geomagnetic polarity time scale. Earth Planet Sci Lett 2004;224:33–44.
[60] Pälike H, Frazier J, Zachos JC, et al. Extended orbitally forced palaeoclimatic records from the equatorial Atlantic Ceara Rise. Quat Sci Rev 2006;25:3138–49.
[61] Li M, Hinnov L, Kump L. Acycle: Time-series analysis software for paleoclimate research and education. Comput Geosci 2019;127:12–22.
[62] Westerhold T, Röhl U, Pälike H, et al. Orbitally tuned timescale and astronomical forcing in the middle Eocene to early Oligocene. Clim Past 2014;10:955–73.
[63] Laskar J, Robutel P, Joutel F, et al. A long-term numerical solution for the insolation quantities of the Earth. Astron Astrophys 2004;428:261–85.
[64] Li Z, Zhang YG, Torres M, et al. Neogene burial of organic carbon in the global ocean. Nature 2023;613:90–5.
[65] Savin SM, Abel L, Barrera E. The evolution of Miocene surface and near-surface marine temperatures: Oxygen isotopic evidence. In: Kennett JP, editor. The Miocene Ocean: Paleoceanography and Biogeography. Boulder: The Geological Society of America; 1985. p. 49–82.
[66] Bauer JE, Cai W-J, Raymond PA, et al. The changing carbon cycle of the coastal ocean. Nature 2013;504:61–70.
[67] Diester-Haass L, Billups K, Gröcke DR, et al. Mid-Miocene paleoproductivity in the Atlantic Ocean and implications for the global carbon cycle. Paleoceanography 2009;24:PA1209.
[68] Holdgate GR, Cartwright I, Blackburn DT, et al. The Middle Miocene Yallourn coal seam—The last coal in Australia. Int J Coal Geol 2007;70:95–115.
[69] Wang P, Li Q, Tian J, et al. Long-term cycles in the carbon reservoir of the Quaternary ocean: A perspective from the South China Sea. Natl Sci Rev 2014;1:119–43.
[70] Ma X, Ma W, Tian J, et al. Ice sheet and terrestrial input impacts on the 100-kyr ocean carbon cycle during the Middle Miocene. Glob Planet Change 2022;208:103723.
[71] Holbourn A, Kuhnt W, Regenberg M, et al. Does Antarctic glaciation force migration of the tropical rain belt? Geology 2010;38:783–6.
[72] Hao Q, Oldfield F, Bloemendal J, et al. The magnetic properties of loess and paleosol samples from the Chinese Loess Plateau spanning the last 22 million years. Palaeogeogr Palaeoclimatol Palaeoecol 2008;260:389–404.
[73] Nie J, Garzione C, Su Q, et al. Dominant 100,000-year precipitation cyclicity in a late Miocene lake from northeast Tibet. Sci Adv 2017;3:e1600762.
[74] Nie J, Ren X, Saylor JE, et al. Magnetic polarity stratigraphy, provenance, and paleoclimate analysis of Cenozoic strata in the Qaidam Basin, NE Tibetan Plateau. Geol Soc Am Bull 2020;132:310–20.
[75] Qiang X, An Z, Song Y, et al. New eolian red clay sequence on the western Chinese Loess Plateau linked to onset of Asian desertification about 25 Ma ago. Sci China Earth Sci 2011;54:136–44.

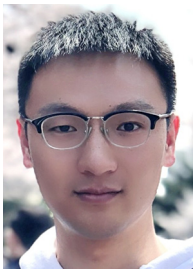

Fenghao Liu received his Ph.D. degree from Tongji University in 2023 and is continuing his postdoctoral research at Tongji University. His research interest mainly focuses on the evolution of astronomically-forced climate changes in Earth's history.

Enqing Huang received his Ph.D. degree from the University of Bremen in 2013 and is currently a professor at Tongji University. His research interest mainly focuses on the geological evolution of low-latitude hydrological cycle and marine carbon cycle.